Multi-Scale Microscopy of Reactive Sintered Boride (RSB) Neutron Shielding Materials

J.M.Marshall[1], F.Tang[2], Y. Han[2], P.A.J. Bagot[3] and M.P. Moody[3]

Department of Physics, University of Warwick, Gibbet Hill Road, Coventry CV4 7AL, UK [1]

Warwick Manufacturing Group, University of Warwick, Gibbet Hill Road, Coventry CV4 7AL, UK [2]

Department of Materials, University of Oxford, Parks Road, Oxford OX1 3PH, UK [3]

*corresponding author j.marshall.4@warwick.ac.uk ORCID: 0000-0003-3642-8968

Protecting superconducting magnets from neutron irradiation is critically important when demonstrating the utility of spherical tokamaks. Reactive Sintered Borides (RSBs) are promising radiation-dense materials and excellent attenuators of slow (< 10 keV) neutrons. No experimental radiation data yet exists on RSBs, hence the need to establish a baseline of RSB microstructure prior to studies on radiation response and aging of RSBs in an active fusion environment.

This work investigates the structure and composition of RSB materials over 5 orders of magnitude. SEM, TEM-EDX, atom probe tomography (APT) and XRD were evaluated the microstructure of a selection of RSB compositions. Sintered RSBs were observed to be dominated by FeWB/FeW_2B_2 bodies, mixed tungsten borides and WC as the key hard phases present. TEM and SEM detected a complex Fe-rich alloy with near-pure Fe interstitial phases. Key findings from this work are that (i) carbon balance is as significant as boron content when considering microstructure and phase presence;(ii) FeWB/FeW_2B_2 growth is highly temperature dependant and (iii) dense, coherent RSB formation is contingent on the total boron and carbon atomic percentage (B + C)at% is $40\% < x \leq 50\%$.

Keywords: Radiation shielding, Nuclear fusion, Tungsten borides, X-ray diffraction, Atom probe tomography

1 Introduction

The development of fusion power is at a critical point driven by recent investigations in tokamak physics [1], advances in high-temperature superconductors (HTS) [2],[3] and the industrialization from ITER [4]. Spherical tokamak designs have been investigated since the 1980's by Peng and Strickler [5] where advantages over conventional toroidal designs including higher plasma current density and smaller foot sizes were observed [6]. The requirement for high field magnets, relative to toroidal tokamaks has limited their application in fusion research until relatively recently. Costley [7] on reviewing tokamaks over a wide range of geometries observed that energy confinement was more weakly dependent on device size than previously assumed. The small size and faster build time of compact Spherical Tokamaks (cSTs) mean considerably fewer resources are required to build reactors than for large toroidal designs, making small, high-field cST reactors a practical path to fusion.

A significant obstacle to practical fusion power is radiation shielding and activation of shielding materials. Investigations on the effect of neutron irradiation on HTS magnets indicated a detectable degradation in performance following relatively modest neutron fluences ($\geq 2 \times 10^{22}$ m^{-2}), equating to less than a week of operation in a 180 MW pilot plant [7],[8],[9]. The compact geometry of a cST makes radiation shielding a challenge. Candidate materials must not activate significantly under irradiation during a duty cycle[10],[11] or remain active for a significant amount of time post-irradiation. For a cST concept power plant [12],[13] the heat loading on the central column and divertors is anticipated to peak at > 10 MW m^{-2} [9] during steady-state operation. Radiation-induced damage from displacements per atom (dpa) from neutrons and γ-rays is anticipated to be ≥ 100 dpa at the plasma-facing component over the course of a reactor lifetime [9].

Current shielding materials are mostly W-alloy based [13],[14], often with a low-Z coating, e.g. Be-coated W metal in JET and ITER [15],[16] [17]. Such alloys have suitable radiation attenuation and mechanical properties for experimental reactors but are not suitable for power-generating reactors [9],[14],[15]. Cemented tungsten carbides (cWCs) are a potential solution for compact fusion shielding. WC combines high- and low-Z elements desirable for absorption and moderation of neutrons and γ-rays [12],[13],[18] alongside high values of Young's and bulk moduli[19]. WC shields used as neutron shields during the Manhattan Project[20], but cWCs have received little attention as radiation shields as the most common cWC binder alloys are based on the highly activating Co and Ni. Use of a Fe-Cr binary alloy (8wt% Cr, Fe-8Cr) as a Co-substitute [21] for a cWC has solved the activation issue and can be processed as for regular cWCs[22],[23].

Reactive sintered borides (RSBs) were developed from boron additions in FeCr-cWCs in 2016, when it was observed that combining B4C, Fe-8Cr and W metal close to the atomic ratio of W:B:Fe ≈ 1 : 1 : 1 formed dense sintered bodies [21] using the same standard cWC PM route with similar mass loss and three-dimensional shrinkage as cWCs.[20] Low energy neutrons are a significant component of the radiation and heat deposition into the HTS core in a cST [12],[13],[18]. RSBs have advantages over cWCs at lower neutron energies (< 10 keV) as would be expected nearer the HTS core. Previous investigations in silico of a combined cWC-RSB shielding concept indicate that neutron attenuation of a combined cWC-RSB shield is more than two orders of magnitude greater than a cWC-only neutron shield for neutron energies < 10^2 eV [13]. The novelty of RSBs[21],[23] means that most of their engineering properties are unknown and there is no existing data on their radiation response to date.

All existing RSB compositions to date were processed using the same proprietary cWC-based process route [13],[24], since no specific RSB processing route currently exists to date. In previous experimental studies of RSB materials, Marshall et al [24] evaluated the complex phase presence and enabled the calculation of the X-ray derived densities ρ_{XRD} from a selection of RSB compositions. Porosity resulting from non-optimal ramping during the early stages of sintering was the main source of defects in RSB materials, particularly for higher boron-containing RSB compositions where B ≥ 35 at% at weigh-in [24]. The focus of this study is the microstructure of the RSB material with the highest density to date (ρ^*/ρ_{XRD} > 98%) over 5 orders of magnitudes, incorporating optical, SEM-EDX, TEM-EDX and Atom Probe Tomography (APT). Microstructural data was correlated with existing X-ray models [24] with APT data enabling X-ray models to be corrected to better reflect the observed microstructure and phase presence revealed by TEM-EDX and APT and to establish a baseline for microstructure in RSBs prior to radiation studies.

2 Method

2.1 Sample preparation and selection

Test materials were produced by a laboratory-scale industrial PM process used for cWC quality control samples[22],[23],[24],[25],[26]. RSB powders were milled using cWC milling media with a media : charge ratio of 9 : 1 in ethanol for 8 hours. A 2wt% addition of polyethylene glycol (PEG) of average mMass = 3400 Da was added to the powder charge prior to milling as a pressing aid. Milled RSB powders were dried, sieved and uniaxially pressed into a variety of test piece geometries with green dimensions 25 x 8 x 6 mm, 20 x 20 x 8 mm and plate samples 50 x 30 x 6 mm. Samples were sinterHIPed at 50 bar under an Ar atmosphere at 1450°C for 1 hour following a standard cWC Ar/H_2 de-binding cycle to remove the 2 wt% PEG addition. Density was measured using the Archimedes

method using a modified Precisa 125 balance with an uncertainty of ± 0.1 mg. Four RSB compositions (B4TE21W, B5T522W, B7TE23W and B9TE25W) were examined by Marshall et al [24], of which three compositions (B5T522W, B7TE23W and B9TE25W) formed dense solid RSB bodies with reasonable mechanical properties. Composition B4TE21W formed a friable, brittle material [24] and was not assessed further in this study. RSB sample nomenclature is composition dependent, with compositions labelled as BXTEyW or BXTxyW, where x = B_4C wt% at weigh-in, and the T in TE acts as a decimal place for B_4C. The quantity y refers to the weigh-in quantity of Fe-8Cr alloy in wt% and W indicates W metal to balance. Compositions and reagent weigh-in quantities of cWC-based and RSB-type materials respectively are shown in Table **1.**

Table 1 Reagent weigh-in quantities for RSB materials in wt%

Sample	Weigh-in wt%				Analysis	Refs
	WC	Fe-8Cr	B_4C	W		
B4TE21W	0	21	4	75	-	[24]
B5T522W	0	22	5.5	72.5	Bulk, XRD, APT	[13],[24]
B7TE23W	0	23	7	70	XRD	[13],[24]
B9TE25W	0	25	9	66	XRD	[13],[24]

Atomic wt% of RSB compositions at weigh-in calculated from **Table 1** are shown in **Table 2**.

Table 2 Atomic wt% breakdown for RSB compositions from **Table 1.**

Sample	Weigh in wt% (Table 1)					
Composition	W	C	Fe	Cr	B	Refs.
B4TE21W	75.0	0.9	19.4	1.6	3.1	[24]
B5T522W	72.0	1.2	20.8	1.7	4.3	[13],[24]
B7TE23W	70.0	1.5	21.3	1.7	5.5	[13],[24]
B9TE25W	66.0	2.0	23.1	1.9	7.0	[13],[24]

2.2 SEM-EDX, ICP, XRD and atomic abundance in sintered materials

Determination of the atomic composition of sintered RSBs is complicated by the presence of low-Z elements mixed with medium and high Z elements. There is also the issue in that RSBs in this work have not been made by an optimized process and have a considerable degree of compositional inhomogeneity particularly with respect to carbon content [27]. The baseline atomic content of sintered RSBs is required since one of the main restraints used in X-ray models is that the composition derived from the X-ray models is consistent with the sample chemistry [24].

Determination of the atomic composition of sintered RSBs is complicated by the presence of low-Z elements mixed with medium and high-Z elements. There is also the issue that RSBs in this work

have not been made by an RSB-specific process and have a considerable degree of compositional inhomogeneity particularly with respect to carbon content [27]. The baseline atomic content of sintered RSBs is required since one of the main restraints used in X-ray models is that the composition derived from the X-ray models is consistent with the sample chemistry [24].

SEM-EDX analysis used a Zeiss SUPRA 55VP system with an Oxford Instruments DryCool Energy Dispersive X-ray (EDX) system with AZTec acquisition and post-processing software. EDX has reasonable accuracy for elements where Z > 10, which is problematic for establishing B and C abundance in sintered materials [28]. Alongside elemental mapping from SEM-EDX, attempts were made to determine representative atomic abundances from RSB compositions B5T522W, B7TE23W and B9TE25W from averaged elemental abundances over 10-12 discrete areas ~3-5 µm wide. EDX-derived atomic presence (wt%) enhanced the signals for C, B and Cr at the expense of Fe and W, with Cr having the largest disparity between detected quantity and quantity at weigh-in. While there is reasonable separation of the key K-peaks for Cr and Fe at 5.948 keV and 6.404 keV respectively and for the nearest W M-peak at 7.388 keV, it is the K-shell peaks for B (0.183 keV) and C (0.277 keV) that are the most ambiguous when compared to the low-energy peaks for W at 0.222 keV. The net result is that W artificially enhances the B and C signals from EDX, given that low-Z elements have a weak signal. EDX cannot be used as a quantitative method for assay for RSBs alone.

To correct for the limits of EDX, powdered RSB samples were analysed by Inductively Coupled Plasma (ICP) to determine the abundance of B and C in sintered materials [this work,[24]). Prior work by Windsor et al [13] also used CONS determination via gas chromatography to measure carbon abundance as a comparison to the ICP-derived values of C wt%. This work assumed that the atomic abundances of Fe, Cr and W present in sintered materials do not change significantly from the weigh-in quantities since Fe, Cr and W are not anticipated to volatize significantly above measurement uncertainty limits over the duration of liquid phase sintering. The light elements C and B do volatize significantly at T > 1000°C and are expected to change in abundance above uncertainty limits. This was the same set of assumptions used in previous work [24] which did not investigate the limits of EDX to the extent of this work. EDX-derived, ICP and CONS-determined atomic wt% are shown in **Table 3**.

Table 3 Comparison of atomic mass % of sintered RSBs measured by EDX, ICP and CONS determination (C only).

Sample	**EDX Abundance wt%**					**ICP wt%**		**CONS wt%**
Composition	**W**	**C**	**Fe**	**Cr**	**B**	**C**	**B**	**C** [13]
B5T522W	49.8	11.1	17.6	9.8	11.2	1.2	4.7	0.8
B7TE23W	50.1	16.8	14.7	9.4	9.1	0.8	5.2	1.0
B9TE25W	45.9	11.0	14.9	16.7	11.0	1.0	5.5	1.4

The ICP-derived values of C and B content from sintered RSBs in **Table 3** are much closer to the calculated values of C and B abundance in **Table 2** from the weigh-in compositions of RSBs than the EDX-determined quantities. The CONS data for carbon content is consistent with the C content at weigh-in and the ICP-derived C data than that from EDX. From this data, it is assumed that using the known quantities of W, Fe and Cr at weigh-in combined with the measured quantities of B and C from sintered materials provides a suitably accurate baseline for X-ray modelling given the limitations of measurement and the compositional inhomogeneity of RSBs themselves.

2.3 TEM-EDX and APT sample preparation

TEM samples were prepared from fragments of composition B5T522W material by mechanical polishing followed by Ar ion milling. TEM-EDX analysis on RSB was performed on a JEOL ARM200f TEM, operated at 200 kV, equipped with an 100 mm^2 windowless Oxford Instruments EDX detector. Atom probe samples were prepared from the polished surface of a sample of RSB composition B5T522W using a SCIOS dual-beam FIB-SEM at the University of Warwick. Samples were FIB milled from a cantilever under protective Pt deposition and then lift-out onto copper tip coupon. Six atom probe specimens were milled in total, of which 5 were viable. APT analysis was performed using a Cameca LEAP 5000XR at the Department of Materials, University of Oxford. APT specimen were analyzed at 50 K at energies 60 – 120 pJ with ion abundances varying from $2.9 \times 10^6 < x < 4.1 \times 10^7$ ions per tip.

2.4 X-ray diffraction modelling in TOPAS

Marshall et al [24] used X-ray diffraction to investigate phase presence and hence theoretical density ρ_{XRD} for a selection of RSB compositions. Prior to this, theoretical density was calculated from the weighted average of reagents [13] which is only applicable if no significant phase formation occurs during sintering as is the case for cWCs. Constraints used for these models were (i) the target atomic abundance derived from selected models deviated from the calculated ICP-adjusted atomic compositions at less than ± 1.0 at% for each species; (ii) the weighted average density $\rho_{XRD} > \rho^*$ and (iii) the weighted Bragg factor RWP at a global minimum for a given model, providing (i) and (ii) are fulfilled, as used by Marshall et al (2020)[24]. Compositions investigated were B5T522W, B7TE23W and B9TE25W using X-ray data obtained from the polished solid surfaces of samples.

TEM-EDX and APT data was used to further refine X-ray models of RSB compositions B5T522W, B7TE23W and B9TE25W using new data on phase presence alongside X-ray models based on phase abundances from Marshall et al [24]. When considering the number of phases per model, this study aims to select the model which has the least number of phases for the lowest given RWP to avoid

overly complex models with artificially low RWP [29]. Restraints refer to parameters within individual phases, were that lattice parameters could vary ± 2% of reference values and atom positions by ± 0.05

3 Results

3.1 SEM-EDX element mapping of RSBs

A series of element maps for B5T522W is shown in **Fig. 1.**

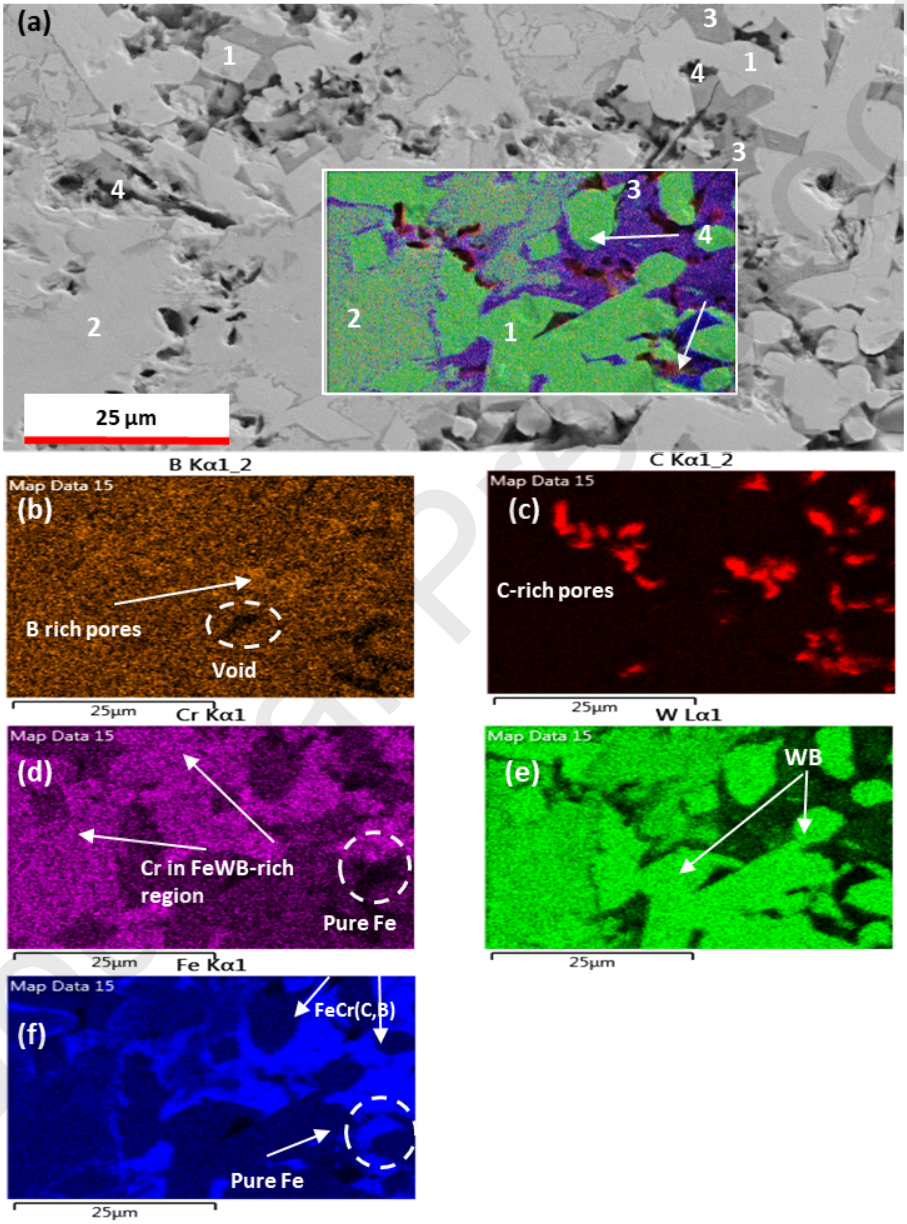

Fig. 1. SEM-EDX maps from RSB sample B5T522W. **a** SE image with combined X-ray maps, **b** B Kα1-2, **c** C Kα1-2, **d** Cr Kα, **e** W Lα1 and **f** Fe Kα1. Preliminary phase-field identification are (1) Tungsten Boride WB/W_2B_5; (2) FeWB; (3) Iron boride and (4) C-rich simple borides and carbides around pores. Pure Fe region is defined by Cr absence (**d** and **f)**.

Cr appears detectable almost everywhere apart from discrete areas highlighted in **Fig. 1d** and **Fig. 1f**. This implies that Cr generally does not segregate significantly into Cr-rich phases and is present within iron tungsten borides in similar concentrations as from weigh-in. Comparing **Fig. 1d** and **Fig. 1f** shows that regions of relatively pure Fe exist as discrete regions within the microstructure. Similar Cr, C and B-depleted Fe regions are also observed in element maps from RSB B7TE23W in **Fig. 2** and B9TE25W in **Fig. 3** respectively. The highest Z-contrast that correlated with the strongest W signal with no significant C signal was assigned as WB/W_2B_5 (phase 1, **Fig. 1)**

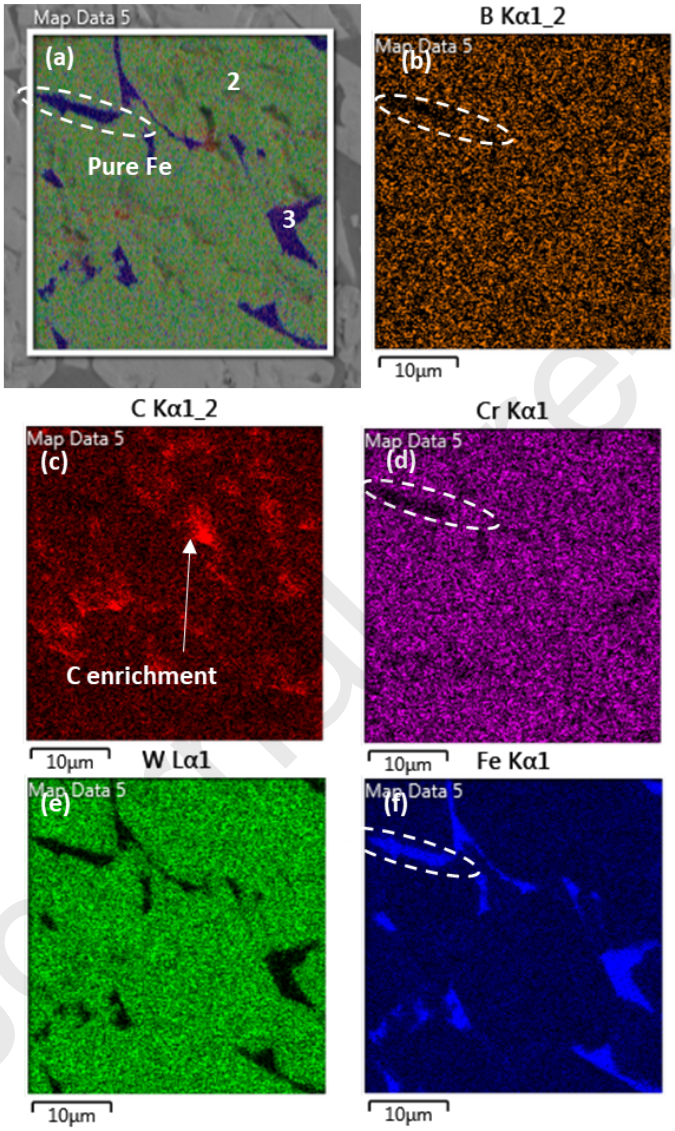

Fig. 2. SEM-EDX maps from RSB composition B7TE23W. **a** SE image with combined X-ray maps for B7TE23W, **b** B Kα1-2, **c** C Kα1-2, **d** Cr Kα, **e** W Lα1 and **f** Fe Kα1. Only 2 main phases are present (2) FeWB and (3) Fe-rich/Fe.

Samples of compositions B7TE23W resembled a pseudo-binary structure within RSB materials in that Fe-rich phase and iron tungsten borides are the dominant phases relative to other phases present [24]. Regions of relatively pure Fe are observed between iron tungsten boride grains within the white ellipse in **Fig. 2b-f**, consistent with observations made of the Fe-rich phases in composition B5T522W. Carbon segregation was observed at FeWB grain boundaries and on grain surfaces as seen in **Fig. 2c.** No Cr segregation and or discrete Cr-rich phases was detected as for B5T522W, indicating that chemically Cr behaves as Fe in iron tungsten borides such that FeWB = Fe(Cr)WB.

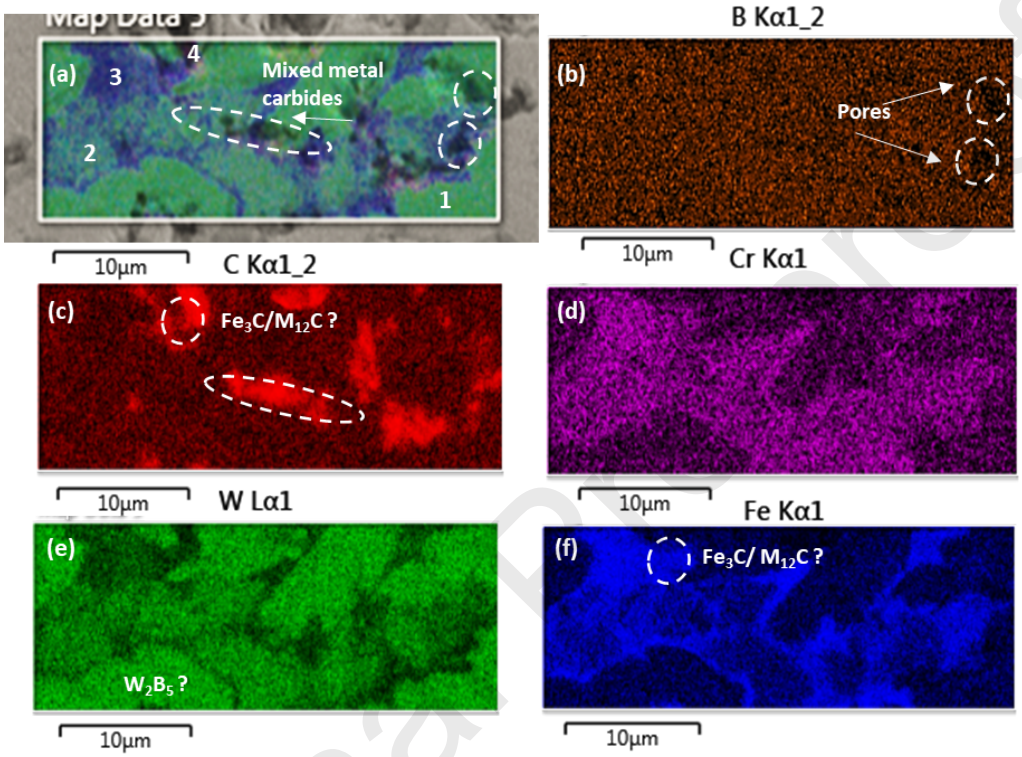

Fig. 3. a SE image with combined X-ray maps for B9TE25W, **b** C Kα1-2, **c** Fe Kα1, **d** Cr **e** W Lα1 and **f** Fe Kα1. The same phases are present as seen in **Fig. 1.** with the possible addition of mixed metal carbides $Fe_3C/M_{12}C$ (1) Tungsten Boride WB/W_2B_5; (2) FeWB; (3) Iron boride and (4) C-rich simple borides and carbides around pores.

Composition B9TE25W (**Fig. 3a.**) has a superficially similar structure to B5T522W in **Fig. 1.** In contrast to B5T522W, the phase field and element maps are less well defined with areas of mixed composition that could include mixed metal carbide ($M_{12}C$, CrC_x and FeC_x) alongside FeWB-dominant areas highlighted in **Fig. 3a.** and that there is a more complex phase field in B9TE25W than B5T522W.

3.3 TEM-EDX imaging

Bright-field (BF) and annular dark-field (ADF) STEM imaging and EDX analysis were focused on the interfacial regions at the WB/FeWB/Fe-rich interfaces of the RSB composition, with results shown in **Fig. 4.**

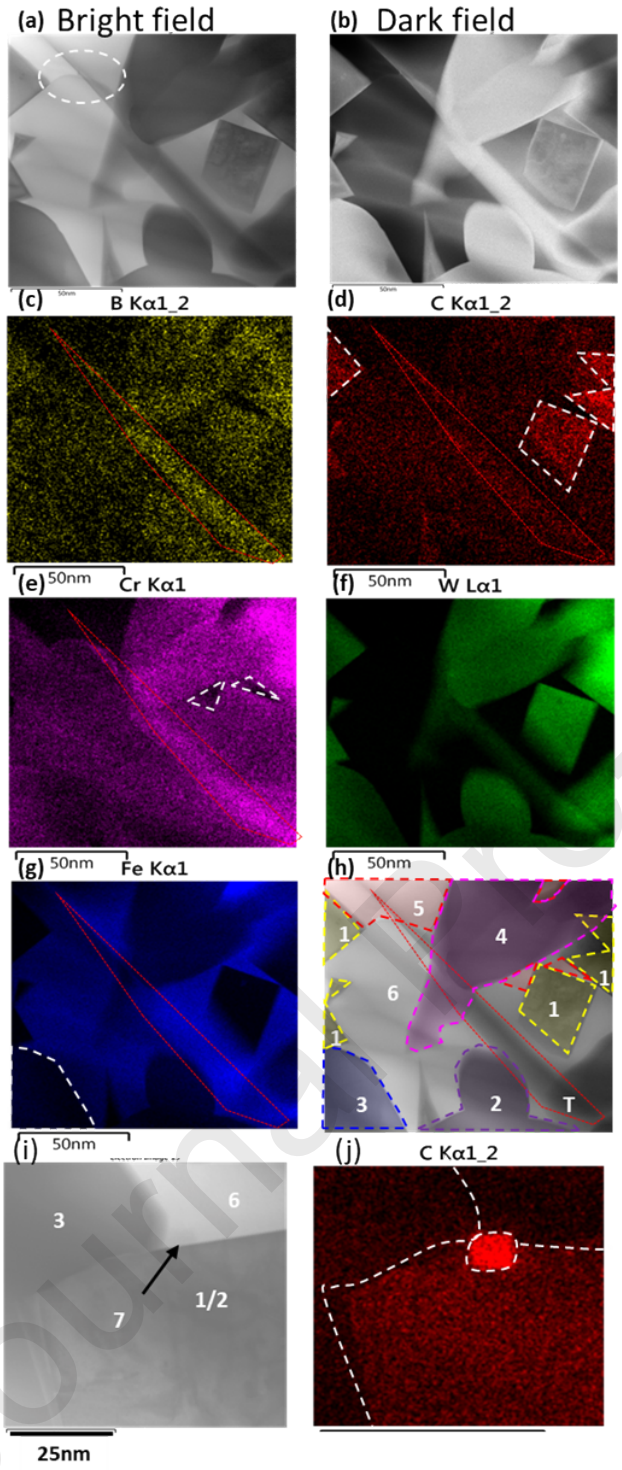

Fig. 4. a BF-STEM image, **b** ADF-STEM image and **(c-h)** TEM-EDX elemental maps from RSB composition B5T522W. EDX maps extracted from **c** B-Kα, **d** C-Kα, **e** Cr-Kα, **f** W-Lα, **g** Fe-Kα and **h** DF image overlayed with region key: (1)WC, (2)W_2B_5/WB, (3)WB, (4)FeWB/FeW_2B_2, (5)Pure Fe (Cr-depleted)(6) Fe(B,C)$_x$, (T) Thicker region. Ringed area in **a** shows the Fe(B,C)$_x$/Fe interface. Images **i** and **j** show evidence of mixed WC/W_2B_5 epitaxy **i** from the textured appearance in region (1/2) and a small C-rich crystal (7) present in **b**.

TEM-EDX maps shown in **Fig. 4.** revealed six distinct phase types, following on from SEM-EDX images in **Fig. 3.** Tungsten boride grains with a more prismatic appearance were associated with carbon presence, with the prismatic features consistent with WC morphology. The presence of dislocations within the grain attributed to W_2B_5/WC in **Fig. 4a-i.** is evidence there is epitaxial growth between WC and W_2B_5, as seen in the terraces present in **Fig. 4a-b**. Rounder tungsten boride grains (2. WB/W_2B_5) are lacking in carbon and have a more diffuse interface with the main Fe-rich phase (6. FeCr(C,B)) than WB/W_2B_5. Carbon maps (**Fig. 4d-j.**) distinguished carbon-containing WC/W_2B_5 crystallites from tungsten borides with no detected C presence (3. WB) **(Fig .4f-g).** The final W-rich phase has considerable Cr and B presence with significant Fe content but no carbon intensity relative to the background and is tentatively identified as FeWB/FeW_2B_2 (4. FeWB/FeW_2B_2). Cr does not show any significant depletion in the FeWB/FeW_2B_2 phase, consistent with SEM-EDX maps **(Fig. 1 – 3).** There is no definitive evidence that discrete M_6C/$M_{12}C$ phases present in composition B5T522W.

The two discrete iron-rich phases (FeCr(C, B))/Cr,B, W-depleted Fe) were observed as seen in **Figs. 2- 3**, with a phase boundary, observed in **Fig. 4a**. **Fig. 4i-j**. shows a carbon-rich crystallite in the interstitial space between a W_2B_5/WB grain boundary and the FeCr(C, B) alloy. This indicates that simple carbides can form at boride grain boundaries as well as at B, C-rich porous defects. The size and morphology of crystallites show a pseudo-fractal structure within the RSB material in that WB/WC/FeWB grains show similar morphologies and distributions over four orders of magnitude (100 nm – 0.1 mm).

3.4 Atom probe tomography

Tips for APT were milled from a region of B5T522W sample surface incorporating regions tentatively identified by SEM as Fe alloy/Cr, B-depleted Fe, WC and FeWB/FeW_2B_2 respectively. The region of interest on the B5T522W sample and the Pt-coated cantilever structure where APT tips were milled are shown in **Fig. 5.**

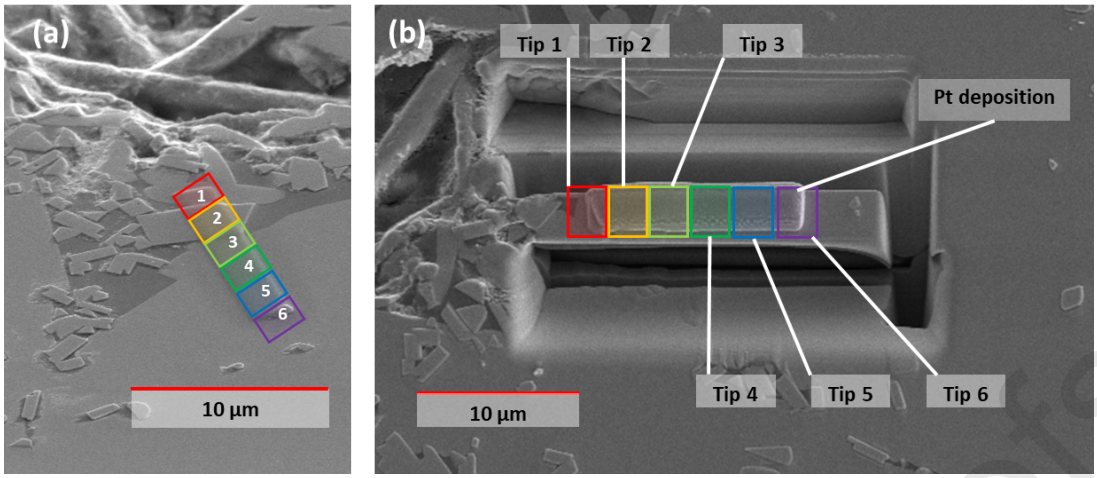

Fig. 5. APT tip location on RSB sample **a** prior to FIB/Pt deposition and **b** Pt-coated cantilever prior to sectioning and shaping.

Atom probe data was obtained from 5 out of 6 APT tips obtained from the region marked in **Fig**. **1**. **Table 3** shows the APT probes ion yield, energy and predicted phases.

Table 4 APT Tip order, atomic abundance and detected phase presence from viable APT tips from RSB B5T522W.

Tip no.	Fe	B	C	Cr	W	Mn	Co	P	N	Cu	Predicted phase	Dominant phase
1	74.7	11.4	6.4	5.0	1.6	0.63	0.21	0.03	0.02	0.01	Fe, FeB_x	Fe-8Cr(C,B)$_x$
2	0.04	0.04	48.3	0.05	51.5	-	-	-	0.02	-	WC	WC
3	24.9	34.0	0.19	2.95	37.7	0.15	0.07	-	-	-	W_2B_5/WC/FeB_x	FeWB/FeW_2B_2
4	24.8	34.4	0.21	2.84	37.5	0.14	0.07	-	0.01	-	FeWB	FeWB/FeW_2B_2
6	24.4	34.9	0.22	2.84	37.4	0.13	0.07	-	0.01	-	FeW_2B_2	FeWB/FeW_2B_2
XRD	28.1	32.7	6.7	1.9	30.1	-	-	-	-	-	Fe, FeB_x	FeWB/FeW_2B_2

Three out of six tips (Tip 3, Tip 4 and Tip 6) were almost pure iron tungsten boride with an average composition equivalent to $(Fe(Cr))_2W_3B_3$. Tip 2 was pure WC, as predicted from Table **3**. Composition between Tips 3, 4, and 6 is very homogenous and does not show a concentration gradient from the large Fe-rich region in **Fig. 5**, consistent with the contrast in SEM images in **Fig. 2** and **Fig. 3.** Tip 6 was compositionally identical to Tips 3 and 4 as seen in Table **4**. Reconstruction and mass-to-charge-state ratio spectrum for Tip 4 and Tip 1 are shown in **Fig. 6** and **Fig. 7** respectively.

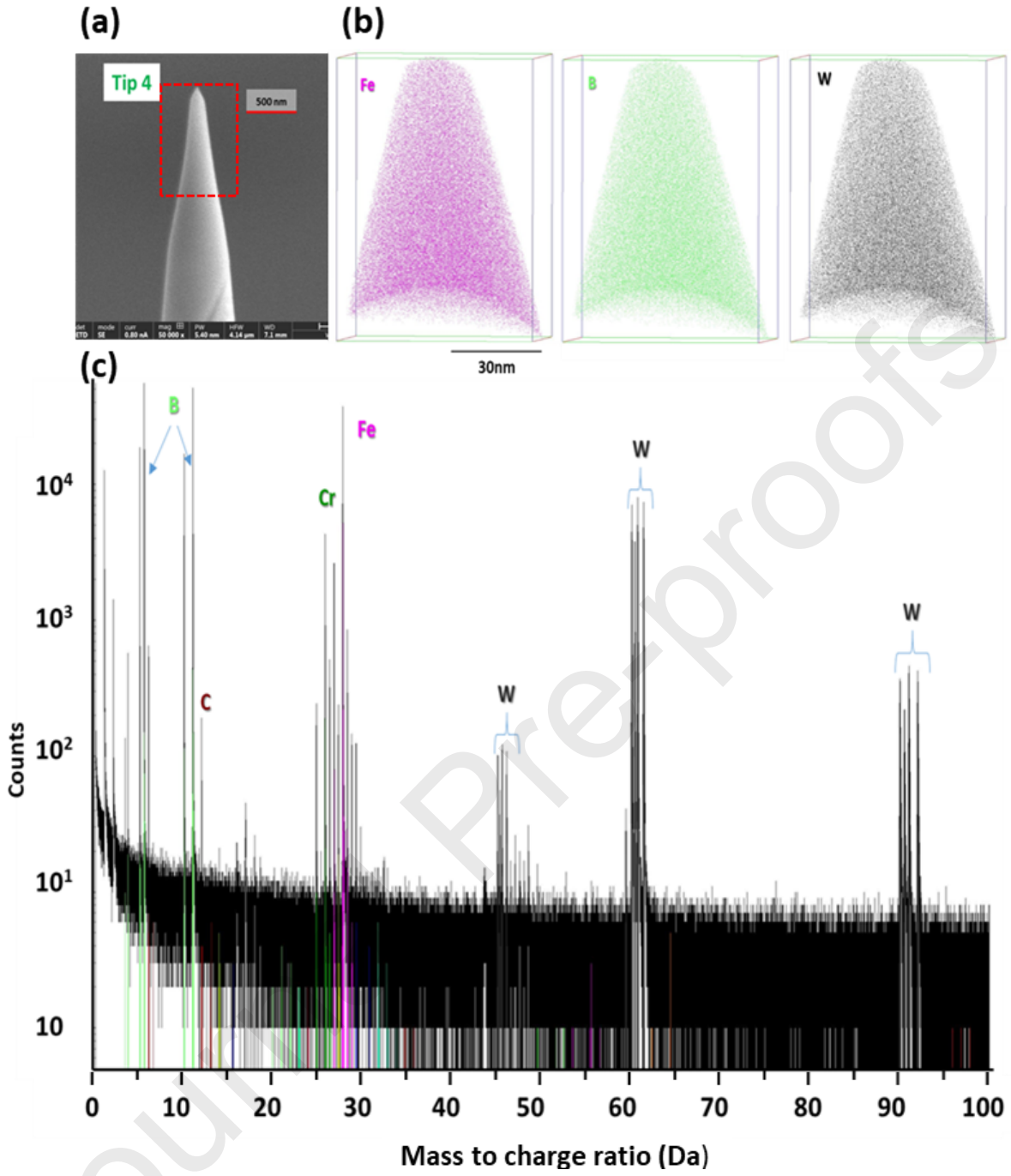

Fig. 6. Atom probe data from Tip 4. **a** SEM image of FIB-milled tip **b** APT reconstruction and **c** mass-to-charge-state ratio spectrum.

Tip 1 was predicted to have some WC/W_2B_5 character, but the region analyzed did not extend to the grain boundary seen in **Fig. 7a**. From the measured atomic abundance for Tips 3, 4 and 6 in Table **4**, no significant Cr depletion was observed within the iron boride tips relative to the Fe-8Cr composition at weigh-in, indicating that Cr does behaves similarly to Fe within the iron tungsten boride phase. The average composition from Tips 3, 4 and 6 is $(Fe_{0.92}Cr_{0.08})_2W_3B_3$, which is a match for an equimolar mixture of Fe(Cr)WB and $Fe(Cr)W_2B_2$. This is confirmed by the mass-to-charge-state ratios

in **Fig. 6c** which shows no significant Cr depletion or segregation within the Fe(Cr)WB/ Fe(Cr)W_2B_2 phase field. **Fig. 7** shows the reconstruction and mass-to-charge-state ratio for Tip 1.

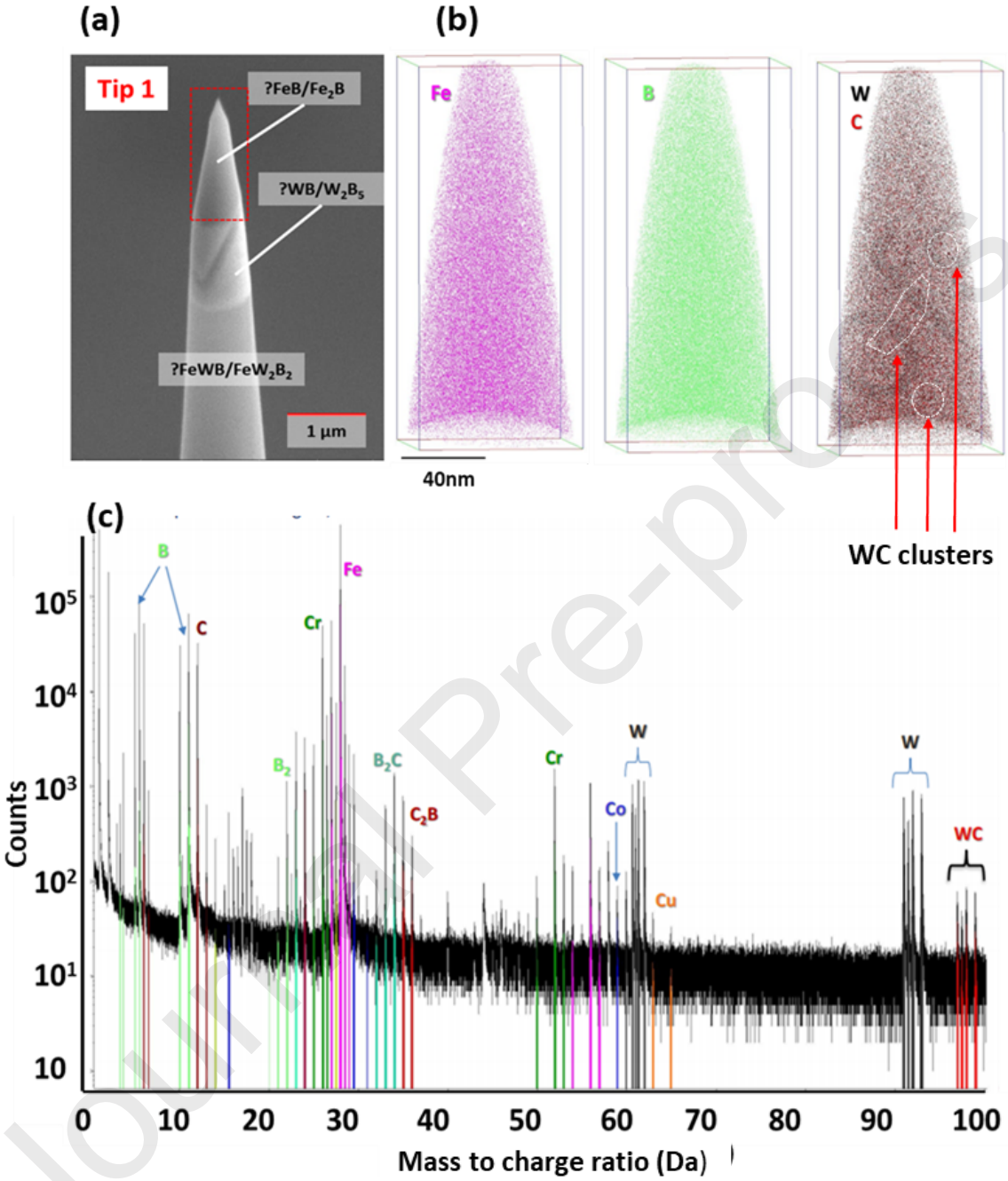

Fig. 7. Atom probe data from Tip 1. **a** SEM image of FIB-milled tip **b** APT reconstruction and **c** mass-to-charge-state ratio spectrum.

The mass-to-charge-state ratio from **Fig. 7c.** shows a complex spectrum with peaks corresponding to mixed borocarbide ions B_2C^+, C_2B^+ and B_2^+, consistent with the presence of nanoscale carbon-rich crystals observed in **Fig. 4j**. WC^+ ions were detected in the mass-to-charge spectrum from Tip 1. No structures indicative of phase boundaries within Tips 3, 4 and 6 were observed indicating no discrete iron borides within Fe-rich phase fields, nor were any structures attributable to

iron(chrome)borides in Tip 1. WC clusters a few atoms wide are highlighted in the tomograph in **Fig. 7b.** and confirmed by the detection of WC^+ ions in **Fig. 7c**.

Cr presence in the FeWB-dominated Tips 3, 4 and 6 was present at similar quantities to the Fe-8Cr alloy powder used at weigh-in, with no significant Cr segregation detected anywhere in this phase. The atomic assay for Tip 1 shown in Table **4** indicates that the Fe-rich zone is closest to a disordered $Fe(Cr)(B,C)_x$ alloy, with W as a trace constituent. No evidence of any iron boride compound was detected in Tip 1. The simplest phase field was obtained from Tip 2 as shown in Table **4** was predicted as WC and confirmed as WC by APT from the prismatic nature of the grain in **Fig. 1**.

The small volume available for APT analysis cannot be assumed to be fully representative of the global composition of the B5T522W sample, but certain trends are evident from SEM, TEM and APT data. These include: (i) No definitive evidence of any detectable FeB_x phase presence (ii) No preferential segregation of Cr in any Fe,W,B – containing phase and (iii) No definitive evidence of $M_{12}C$/FeWB coexistence or $M_{12}C$ presence. This indicates that the carbon segregates to four discrete phase fields in this RSB material. In order of significance, these are: WC, FeCr(Cr,B) alloy, other simple carbides (FeC_x, CrC_x BC_x Fig. 4) and free carbon (**Figs. 1 - 3**).

3.5 X-ray models for RSB compositions post-analysis of B5T522W

Initial X-ray models used by Marshall et al [24] had a large number of phases present to ensure models matched the observed atomic abundance and fitted the criterion $\rho_{XRD} \geq$ measured density (ρ^*) [24]. Models in this work applied an iterative approach, removing phases that did not refine or contribute to minimizing RWP, without compromising sample chemistry or $\rho_{XRD} \geq \rho^*$. Trace phases (< 0.5 mol% were included if they significantly contributed to reducing the RWP factor. In this study, 17 phases were observed to account for significant diffracted intensity and affect the goodness-of-fit (GoF) of the X-ray models. Alongside the complex Fe-rich phase modelled as $(Fe_{0.92}Cr_{0.08})_{22}B_4C_2W$ based on $Fe_{22}B_6W_{0.8}$ (Group 225, *Fm-3m*) from PDF 01-075-2992. The complex Fe-rich phase was modelled with C substituting for B at B positions, two different Fe(Cr) positions and a shared W,Cr site based on the shared Fe,W site from the original PDF as shown in the TOPAS model in **Fig. 9.**

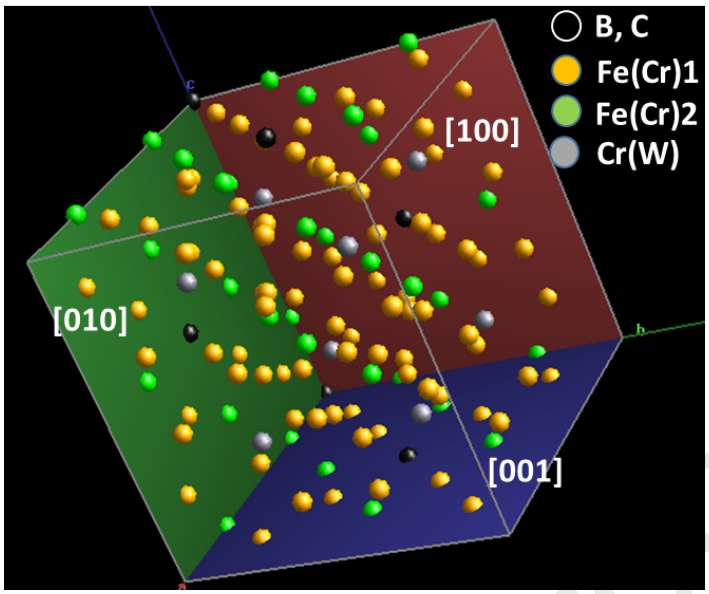

Fig. 8. TOPAS model of complex as $(Fe_{0.92}Cr_{0.08})_{22}B_4C_2W$. Fe(Cr)1 has occupancy of $Fe_{0.9}Cr_{0.06}$ and Fe(Cr)2 has occupancy of $Fe_{0.9}Cr_{0.1}$ respectively. Silver sites are the shared $W_{0.43}Cr_{0.57}$ site with B and C sharing the original B site.

The complex (Fe,Cr)B,C phase assumes that the original shared W,Fe site would have Cr substituting for Fe since W and Cr are Group VI elements and any Cr segregation occurring would favour W-sites more than Fe-sites if such a situation arises. Other additional phases include Fe_3B (PDF 04-013-1369) and WB_2 (PDF 01-086-3955) in light of the current uncertainty over the exact composition of W_2B_5 [30]. Despite the initial complexity, RSB X-ray models observed that the 75% < x < 95% of diffracted intensity from all RSB compositions could be attributed to four main phase types: (1) Iron tungsten borides; (2) tungsten borides; (3) Fe-rich alloys and (4) tungsten carbide.

For the pre-APT solid surface RSB models, assumptions used were that the bulk of the Fe-rich interstitial phase was composed of mixed iron borides (FeB_x) alongside the B, Cr-depleted Fe bcc. Post-APT, FeB_x and intermetallic phases were eliminated with a new unit cell based for $(Fe_{0.92}Cr_{0.08})_{22}B_4C_2W$. Compositional data from SEM, TEM-EDX and APT analysis from B5T522W enabled X-ray models to be updated for composition B5T522W. For compositions B7TE23W and B9TE25W, their X-ray models were updated as for composition B5T522W. Since the APT probes were fabricated from the sintered surface of B5T522W, only the surface (solid) compositions were revised in this work. comparing pre- and post-APT models for compositions (a) B5T522W, (b) B7TE23W and (c) B9TE25W are shown in **Fig. 9**.

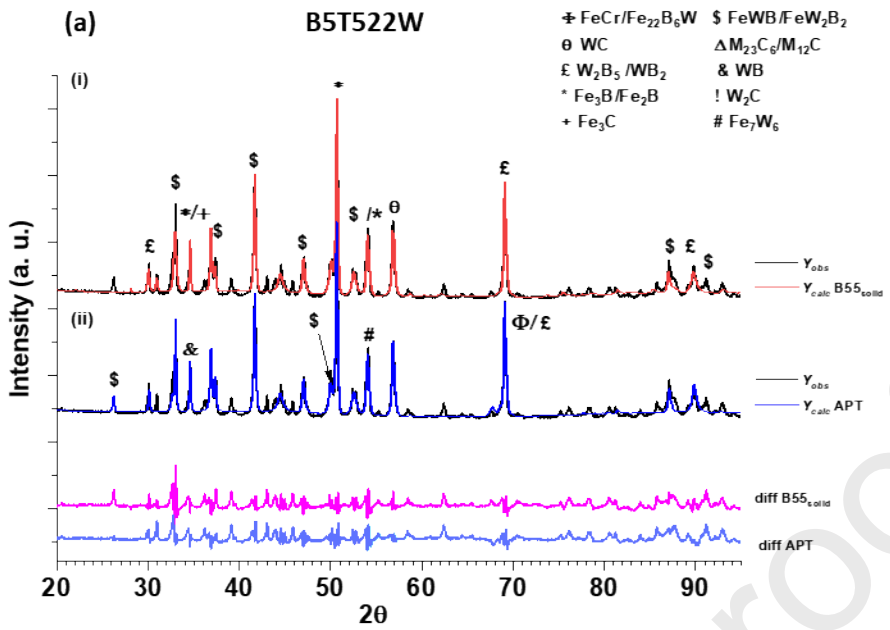

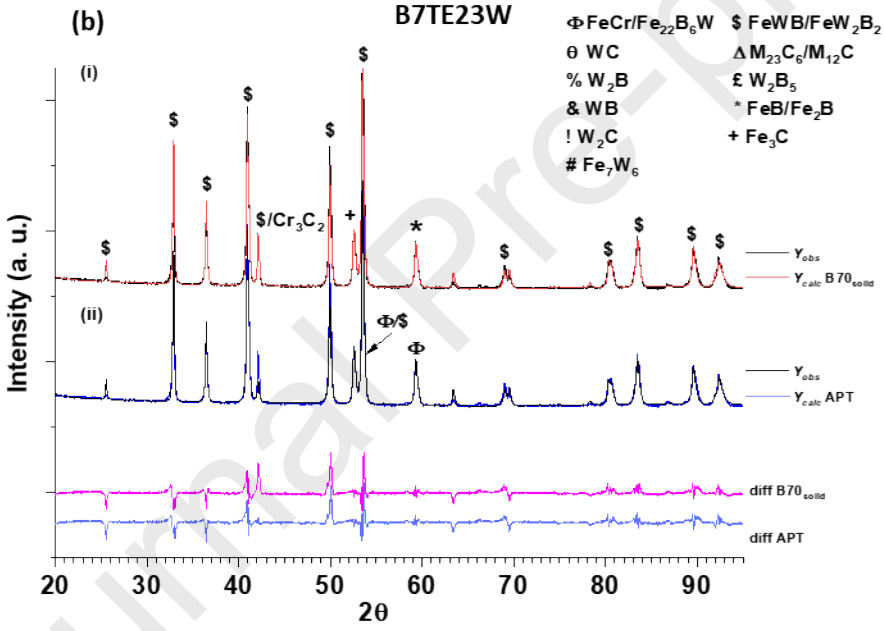

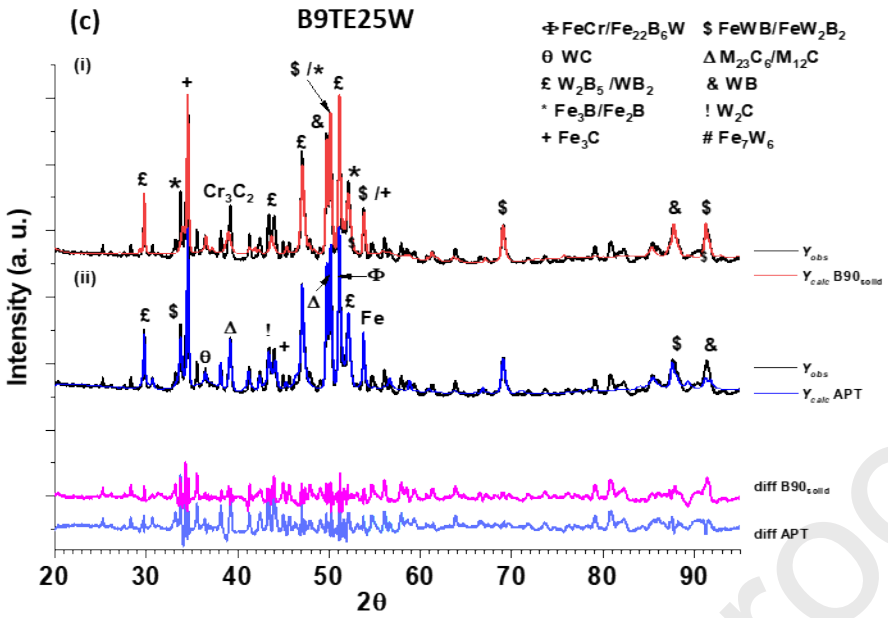

Fig. 9. X-ray model fits of RSB surface spectra from **a** composition B5T522W, **b** B7TE23W and **c** B9TE25W. Fits show (i) models using iron borides and (ii) models using the bcc (Fe, Cr)(B, C) ($(Fe_{20}Cr_2W)B_4C_2$) Fe-rich alloy discovered from APT analysis. For clarity, only peaks in the solid spectra differing from the powder data are labeled.

Most models that had suitable average densities, atomic abundance and local minima in RWP tended to converge on compositions that were slightly carbon deficient and W and Fe-enriched relative to powder compositions [24]. RSBs, similar to cWCs usually have a surface that is carbon deficient relative to the bulk [24],[31],[32],[33]. Phase abundance and GoF (R_{wp}/R_{exp}) from X-ray models from **Fig. 9.** are shown in Table **5**.

Table 5 Phase abundance and goodness-of-fit (GoF) from RSB X-ray models comparing pre- and post-APT derived models.

Phases	B5T522W		B7TE23W		B9TE25W	
Mol %	B55 solid	B55 APT	B70 solid	B70 APT	B90 solid	B90 APT
$Fe_{0.92}Cr_{0.08}W_2B_2$	30.64	30.44	74	72.32	19.05	32.18
$Fe_{0.92}Cr_{0.08}WB$	23.9	34.76	0	0	12.34	8.07
Fe_3B	1.1	0	0	0	14.43	0
Fe_2B	7.88	0	12.28	0	10.59	0
WB	5.64	4.79	0	0	3.82	4.82
WB_2	0.57	0.46	0	0	3.49	2.96
W_2B_5	6.19	6.29	0.83	4.05	17.67	14.2
Cr_3C_2	1.6	0	2.29	0.79	2.22	0
WC	8.85	6.58	0.28	0.31	8.94	2.1
$M_{12}C$	0	0	0	0	2.22	1.33
W_2C	0	0	0	0	0	1.27
Fe_7W_6	6.88	1.49	0	0	2	0
$M_{23}C_6$	0	0	0	0	0	1.5
Fe_3C	6.66	9.51	8.23	8.58	5.5	4.3
Fe	0	0	0.5	0.38	0	0.3
$(Fe_{20}Cr_2W)B_4C_2$	0	5.67	0	12.64	0	26.2
graphite	0	0	1.73	0.98	0	0.8
GoF (R_{wp}/R_{exp})	6.489	5.000	3.784	3.944	6.177	5.443

X-ray models for RSBs pre-and post-APT analysis show that FeWB/FeW_2B_2 is the most common phase present in all three compositions. In the case of composition B7TE23W, FeW_2B_2 is the *de facto* dominant phase accounting for almost 75% of the diffracted intensity, with Fe-rich phases accounting for 10-13% and other phases only accounting for the remaining 10-15% diffracted intensity for composition B7TE23W.

Compositions B5T522W and B9TE25W appear superficially similar in that both have significant iron tungsten boride presence with WB/W_2B_5, WC and Fe-rich phases in the interstices between hard boride bodies. WB/W_2B_5, WC presence accounts for almost twice the diffracted intensity in B9TE25W relative to B5T522W with significantly reduced iron tungsten boride presence relative to B5T522W. B9TE25W has the most complex phase presence in terms of attributed diffracted intensity and microstructure. Atomic abundances and ρ_{XRD} of legacy X-ray models [24] and models shown in Fig. **9**. and from the phase abundance in Table **5**. are shown in Table **6**.

Table 6 Atomic abundance, X-ray density ρ_{XRD} and percentage density ρ^*/ρ_{XRD} from RSB X-ray models.

Model	XRD – derived abundance at%					ρ_{XRD}	ρ^*/ρ_{XRD}	Ref.
	W	C	Fe	Cr	B	g cm^{-3}	%	
B5T522W	29.89	7.37	27.43	2.39	32.93	12.59	99.3	[24]
B55 solid	32.64	5.64	30.89	2.61	28.12	12.59	99.3	-
B55 APT	33.13	5.34	26.88	2.10	32.56	12.58	99.4	-
B7TE23W	28.38	4.78	28.39	2.47	35.98	12.27	87.0	[24]
B70 solid	29.98	4.84	28.48	2.56	34.29	11.49	92.9	-
B70 APT	29.23	4.48	29.56	2.08	34.67	11.50	92.8	-
B9TE25W	25.71	5.96	29.65	2.58	36.10	11.91	87.2	[24]
B90 solid	25.09	6.89	30.22	2.12	35.73	11.45	90.7	-
B90 APT	25.63	5.57	31.53	2.79	33.70	11.42	90.9	-

The atomic abundance from the X-ray models pre- and post-APT analysis show a more W and Fe-rich composition relative to the legacy composition corrected using ICP data [24]. Overall, atomic abundances were consistent with the atomic weigh-in and the relative carbon deficiency of the surface relative to the bulk in RSBs. The most notable change from X-ray models post revision are the X-ray densities ρ_{XRD} for compositions B7TE23W and B9TE25W. Both sets of revised models showed a lower ρ_{XRD} relative to the legacy ρ_{XRD} [24] and a higher ρ^*/ρ_{XRD} from legacy data for these compositions.

The GoF of models post-APT analysis generally showed an improvement relative to the pre-APT models in Table **5** with the exception of B7TE23W. In the case of the models for B7TE23W, both pre- and post-APT models had the lowest GoF out of all compositions, a reflection of the relatively simple phase field observed from samples of B7TE23W relative to the other RSBs evaluated in this work. In general, APT-based models more closely resembled the ICP-EDX derived data than those with mixed iron borides as the dominant Fe-rich phase presence.

4 Discussion

4.1 Microstructure and RSB compositions

RSBs have highly heterogenous microstructures with the largest feature sizes typically 10–100 µm, 2 orders of magnitude greater than for most cWCs. The largest feature sizes are attributed to FeWB/FeW_2B_2 bodies forming the bulk of the RSB matrix. For B9TE25W, the large FeWB/FeW_2B_2 bodies are largely absent, as are the WC grains embedded in the FeWB/FeW_2B_2 grains as shown in **Fig. 3.** and by Marshall et al [24]. The microstructure of B9TE25W is dominated by shorter 10-20 µm tungsten boride grains in a matrix dominated by a Fe-rich phase.

Samples of composition B5T522W were observed to have relatively low porosity compared to other RSB compositions, with delamination features only being significant for larger wear test

geometries [24]. In contrast, composition B4TE21W the only composition where B content was < 30 at% at weigh-in, was found to be highly friable and lacked cohesion even in small samples [24]. These observations indicates that insufficient boron and carbon additions in RSBs will form sintered bodies dominated by brittle intermetallic phases (Fe_7W_6, also known as μ-phase) and mixed metal carbides (M_6C, $M_{12}C$, $M_{23}C_6$ also known as η – phase). Dense, cohesive RSB bodies did not form if boron content is ≥ 30 at% at weigh-in.

Composition B7TE23W has a microstructure significantly different to either compositions B5T522W and B9TE25W in that it is a pseudobinary structure dominated by two phases, specifically FeW_2B_2 and $(Fe_{20}Cr_2)WB_4C_2$ as seen in **Fig. 2.** WC grains embedded in the FeWB/FeW_2B_2 phase were completely absent in B7TE23W in contrast to other RSBs, as seen in **Fig. 9b**. and Table **5**. It is unclear exactly how B7TE23W has such a dramatically different microstructure when compared to B5T522W and B9TE25W since the sintered composition is not that different to that of B9TE25W and the sintering conditions were the same as for all RSBs evaluated in this work [24]. B7TE23W has significantly less carbon post sintering than B5T522W and B9TE25W (Table **3** and Table **6**) but has almost identical boron composition from the bulk (Table **6**).

There are two probable reasons why B7TE23W lost so much carbon between weigh-in and sintering relative to other compositions. The first one is that initial RSB samples were sintered in a large industrial SinterHIP, so some variance in furnace conditions within the hot zone is a possibility, particularly if samples were placed nearer the heating elements nearer the gas inlets, which could potentially accelerate carbon removal during PEG removal and the hot dwell. Another explanation is that composition B7TE23W itself is close to a composition sweet spot for runaway FeWB/FeW_2B_2 growth once conditions are optimal for iron tungsten boride growth during sintering. Excess carbon would be driven to the FeWB/FeW_2B_2 grain boundaries and edges and the sample surface itself as seen in **Fig. 2**., accelerating carbon loss at sintering temperatures.

If there is a very narrow window for runaway FeWB/FeW_2B_2 growth near T = 1450°C, then relatively minor temperature disparities inside a large SinterHIP furnace could result in highly dissimilar microstructures in RSB samples, despite having similar compositions at weigh-in. Some evidence for this is observed from the APT tips shown in **Fig. 6**. Differences in compositions between Tips 3, 4 and 6 in Table **4** are below uncertainty, indicating a negligible composition gradient between edge and 10 μm from FeWB/FeW_2B_2 grain edge. This is indicative of rapid growth of a compositionally homogenous body through the Fe-rich matrix, consuming boride precursors during growth. Large WC grains are present within iron tungsten boride bodies in B5T522W, indicating that carbon presence hinders FeWB/FeW_2B_2 grain growth.

4.2 Grain growth during RSB synthesis

Carbon presence was observed to have a significant impact on microstructure as seen in **Fig. 2.** and **Fig. 3.** and in Table **6**. Compositions B7TE23W and B9TE25W had very similar B content post sintering but completely different microstructures. The most obvious reason is that B7TE23W is significantly carbon depleted relative to other RSBs in this work and this is reflected in the phase presence. While mixed FeWB/FeW_2B_2 is the dominant phase in RSBs, accounting for > 40% of diffracted intensity even for B9TE25W, they are overwhelmingly dominant in composition B7TE23W accounting for almost 75% of all diffracted intensity, consistent with microstructure in **Fig. 2.** From this work, it is reasonable to assume that explosive FeWB/FeW_2B_2 growth correlates with local regions of low carbon presence. Compositions B5T522W and B9TE25W have more mixed phases and have higher carbon contents than B7TE23W. WC grains are present within most large FeWB/FeW_2B_2 bodies in B5T522W and B9TE25W but are absent in B7TE23W as seen in **Fig. 1**. and **Fig. 5**. The refractory nature of WC and its carbon content ensures that WC grains are the last phase to be consumed by the FeWB/FeW_2B_2 phase. Further examination of **Fig. 1** and **Fig. 3** show that carbon-rich phases surrounding C-rich lacunae appear to hinder FeWB/FeW_2B_2 growth resulting in more WC, W_2B_5 presence and less Fe consumption.

Between organic binder removal and sintering (400°C < T < 1450°C), the first phases to nucleate include cementite (Fe_3C) and WC, since WC nucleation in a Fe-rich media was observed to commence at T ≥ 500°C[34] and Fe_3C forming from T > 250°C [34]. WC nuclei are observed in the APT reconstruction of Tip 1 (**Fig. 7.)** within the Fe-rich phase. The nucleation and growth ranges for common phases detected in RSB materials are shown in Table **7**.

Table 7 Nucleation temperatures for common RSB phases

Phase	Nucleation Range °C	Reference
WC	>500 – 850	[34]
W_2B_5	950 - 1300	[35]
WB	>800 - 1000	[35]
FeB	860 - 980	[35],[36],[37]
Fe_2B	860 - 980	[35],[36]
FeWB	>950-1000	[35]
Fe_3C	250-700	[34]

From Table **7**, Fe and W carbides form first during with WB starting to nucleate at T > 800°C. Iron boride formation commences near T > 860°C [36],[37] with FeWB starting to form at T > 950°C [35]. WB starts nucleating near T = 800°C with the growth rate becoming significant at T > 900°C and W_2B_5 formation initiates near T = 950°C. Assuming that sintering conditions are such that all regents at weigh-in are consumed, WC is expected to be present as large, discrete grains surrounded and FeWB/FeW_2B_2 as observed in composition B5T522W in **Fig. 1.** The presence of large WC grains embedded in a FeWB-dominant matrix is also consistent with the APT area of interest seen in **Fig. 5.** where WC grains are present as discrete grains present throughout both FeWB and Fe-rich phase fields. This indicates that any FeB_x that does form during sintering is consumed by FeWB at T > 1100°C and is not detected in sintered RSBs in this work.

The nucleation of WC at relatively low temperatures could aid nucleation of tungsten borides since there is a reasonable lattice match between the [0001] faces of WC and W_2B_5. Some evidence of mixed WC/W_2B_5 grains is seen from the dislocations and C and B presence in the TEM-EDX maps in **Fig. 4c**. and **Fig. 4d**. respectively. The presence of W_2B_5 could also aid the nucleation of WB once there is less B present following W_2B_5 growth as seen in Table **8**. Lattice matches between WC and W_2B_5/WB and ε-WB_2/W_2B_5 phase proposed by Setayandeh et al [30] are shown in Table **8.**

Table 8 Lattice matching between tungsten boride and tungsten carbide.

Phase	**Lattice Parameters (Å)**							**Group**	**Phase matching**
	a	**±**	***b***	**±**	***c***	**±**	***γ°***		**Parameters (*a,b,c)***
WB	3.263	0.0006	8.536	0.0015	**3.020**	**0.1565**	90	Cmcm	***a*** W_2B_5
WC	2.940	0.0005	**2.940**	**0.0005**	2.829	0.0006	120	P63/mmc	***a*** W_2B_5
W_2B_5	2.986	0.0002	**2.986**	**0.0002**	13.999	0.0027	120	P63/mmc	***a***WC, ***c***WB
ε-WB_2 (W_2B_4)	2.970	0.009	**2.970**	**0.009**	13.898	0.006	120	P63/mmc	***a***WC [30]

The proposed ε-WB_2 phase in Table **8** has lattice parameters close to that of W_2B_5 from PDF 00-030-1385 since the lowest energy configurations of probable ε-WB_2/W_2B_5 phases have diffraction patterns closest to PDF 00-030-1385 [30] also have a reasonable lattice match with WC. However, this is by no means conclusive the most stable ε-WB_2 phase may not have any significant lattice match with WC [42]. If WC does not have any significant impact on ε-WB_2/W_2B_5 nucleation, it is unlikely that it would have a significant impact on sintered bodies since tungsten borides spontaneously nucleates for W/B-rich mixtures [43] with WB nucleating spontaneously for T > 800°C.

Some evidence that FeWB forms from WB reacting with Fe from a relatively carbon-depleted Fe-rich phase is seen in the SEM image of the APT tip zone in **Fig. 5**. In **Fig. 5a.** massive linear structures can be seen where some of the Fe-rich phase field has been preferentially eroded during polishing, leaving structures are mostly WB grains, which form long cuboid crystals as seen in **Fig. 1a.** The rounder morphology of the massive structures indicate that the WB phase is being consumed by the FeWB phase from reaction with the Fe-rich phase. The Fe-rich phase acts to transport different species during grain growth, as for liquid phase sintering in conventional cWCs [22],[25],[26]. FeWB growth and the consumption of Cr, W and B from the Fe-rich alloy could explain the presence of pure Fe lacunae (**Fig. 1, Fig. 2 and Fig. 4.)** observed in WB and FeWB interstitial spaces.

Assuming the first phases to nucleate post-PEG removal are WC and Fe_3C, the Fe-rich matrix would be depleted in carbon first, then W and B depletion from WB and W_2B_5 growth. The lack of composition gradient between the FeWB/FeW_2B_2 APT tips 3, 4 and 6 indicate that the transformation from Fe + WB to FeWB from the following reaction sequence WB + Fe → FeW_2B_2 → FeWB is very rapid at 1450°C.

4.3 Structure-property relationships of RSBs

The combination of high hardness and fracture toughness in cWCs results from the contiguous WC skeleton that forms during sintering [26],[35],[38],[39] and a ductile metallic binder which retards crack growth and enables dislocation migration through the binder phase. RSB materials have a highly complex microstructure relative to cWCs as they are a mixture of different crystalline phases with highly disparate mechanical properties but the properties of B5T522W are consistent with the laws of mixtures [40],[41]. Mechanical properties of B5T522W [13],[24] are similar to fine-grained cWC-based cermets with slightly lower hardness and fracture toughness than most cWCs of 10wt% metallic binder content and d_{WC}- ≤ 1 µm. This corresponds to hardness (Vickers, HV) 15 GPa < HV < 16 GPa and critical stress intensity K_{1c} ,a measure of fracture toughness 8 MPa $m^{0.5}$ < K_{1c} < 9 MPa $m^{0.5}$. Dense, defect-free RSB samples of composition B5T522W are predicted to have mechanical properties, hardness and toughness between that of pure FeWB and the fine-grained cWC materials [22]. Pure dense FeWB as synthesized from elemental powder via spark plasma sintering [35] was recorded as having a maximum HV ≥ 21 GPa and a fracture toughness K_{1c} ≈ 8.3 MPa $m^{0.5}$. Other RSB compositions had significantly lower values of HV and K_{1c} not exceeding 13 GPa and 6 MPa $m^{0.5}$ respectively [24] but this is attributed to the porosity rather than anything microstructure related.

The coexistence and substitution of Cr and Fe has also been observed in Fe, W, Cr precipitates in B_4C-based materials [42], although this work showed that B has a slight preference for forming precipitates with Cr relative to Fe – this would account for the small regions of relatively pure Fe

observed between boride grains. It is therefore possible that even significant increases in the Cr content in RSBs at the expense of Fe would still form Fe(Cr)WB and Fe(Cr)W_2B_2. This is significant in terms of ferromagnetism or corrosion resistance that could be issues with existing known RSB compositions.

A pseudo two-phase FeWB/Fe-rich material would also have reasonable hardness and toughness providing it is fully dense but there are some advantages in a more heterogeneous microstructure as seen in B5T522W in that the long, thin tungsten boride grains could act to pin the FeWB bodies and act as crack deflection. Embedded WC grains in the FeWB bodies would also act as pinning sites. The presence of Fe-rich phases reinforced with WB and smaller FeWB-based bodies would also act as dislocation traps and supply some ductility to the microstructure, albeit in a more de-localized way relative to cWCs.

4.4 Processability of RSBs

This work gives insights into RSB processing in that the target phase constituents and densities are more accurately determined for a wider selection of RSB compositions than just B5T522W. The multi-scale characterization of RSB composition B5T522W reveals a fractal-like structure dominated by iron tungsten boride crystals over the size range >100 μm (**Fig. 1**) to < 100nm (**Fig. 4**), the smaller bodies present within the Fe-rich interstitials between larger bodies with other hard phases (WB, W_2B_5, WC) presence. The net result is that B5T522W forms a skeleton-like structure dominated by a network of iron tungsten boride grains over 4 orders of magnitude. It is anticipated that other RSB compositions would form similar skeleton structures with hard phases and softer phases in the interstitial spaces.

The low density and extensive delamination from both B7TE23W and B9TE25W compositions appear to be consistent with the observation that neither composition B7TE23W or B9TE25W formed such large FeWB/FeW_2B_2 bodies as the dominant matrix, as did composition B5T522W. It is unclear whether the poor densification of compositions with higher boron and carbon contents than B5T522W result solely from non-optimal processing or if it is inherent to the RSB composition itself. Composition B4TE21W had a sintered B at% = 25.5% and did not form a cohesive body in that there was insufficient boride phases to form a cohesive boride framework, not too dissimilar to the WC skeleton in cWCs [6],[25]. It is possible that increasing carbon content in lower boron-containing RSBs would result in a contiguous sintered body. It is possible that (B + C)at% ≥ 40% at weigh-in is a condition for forming a dense, cohesive RSB body from sintering. That is, what is the upper limit of boron and carbon content in an RSB before it cannot be fully densified under pressureless sintering?

When considering the carbon content of cWCs (excluding spark plasma sintering or high pressure high temperature methods), [24],[25],[26] conventionally sintered cWCs have binder contents down to 3 wt%, corresponding to a carbon content of 48.5 at%. The ability of the WC phase in cWCs to form a continuous network of WC/WC grains is what determines the upper limit of binder content, which depends on the density of metallic binder. For Fe-8Cr cWCs this is 25 wt%, corresponding to a total C at% = 37.5 at%, close to the (B + C) at% ≈ 40 at% limit for RSBs. Compositions B5T522W, B7TE23W and B9TE25W have a combined weigh-in B and C at% > 40%, while B4TE21W had a combined (B + C)at% ≈ 30%. If the condition (B + C)at% ≤ 37.5% for any RSB composition, then composition B4TE21W cannot form a cohesive RSB body due to insufficient boron and carbon content.

In terms of the nature of a borocarbide skeleton structure, while there is some evidence of a partial lattice match between W_2B_5 and WC, it is unlikely that tungsten borides would form a WC-like skeleton structure since FeWB/FeW_2B_2 are the dominant sintered phases. Such a boride 'skeleton' would consist of large, interpenetrating FeWB/FeW_2B_2 bodies as seen in **Fig. 1** and **Fig. 5**. It is probable that the upper limit of boron and carbon content for RSB sinterability is similar to that of cWCs in that (B + C)at% ≈ 50%. From this it is possible that boron-only RSBs could be possible or true cWC-RSBs in the case of potential low-B RSBs, where a contiguous cWC skeleton coexists with boride presence. The composition B9TE25W is therefore close to the limits of sinterability at weigh-in.

Current sintering conditions were based on those used for cWCs given that an RSB-specific sintering process is under development. Delamination defects consistent with non-optimal sintering are present in all B5T522W samples with cross-section dimensions greater than 6 mm x 6 mm, some of which are not obvious until cross-sectional sample preparation. Such defects are consistent with either poorly controlled PEG decomposition or with gas release from the reagents themselves at elevated temperatures. Gas release in cermet-type materials can be mitigated by slowing the ramp rate or adding a dwell whenever the gas release is at a local maximum, as is the case for general cWC sintering [43].

PEG is anticipated to interact differently with RSBs relative to cWCs at elevated temperature. A source of gas release is specific to RSBs in that B_4C and elemental boron often has significant oxygen retention since boron oxides forms readily in ambient conditions. This would account for gas release at temperatures (≥ 900°C) significantly higher than those for PEG decomposition, which is complete around 400°C. Systematic analysis of different RSB compositions is required to ascertain how PEG interacts with RSBs relative to cWCs as well as evaluation of gas flux from samples during heating. Given that composition B5T522W shows good densification despite non-optimized processing, such processing issues will be resolvable within conventional PM methods.

5 Conclusions

RSB materials with a selection of boron contents are a credible candidate for fusion shielding applications and can be processed using conventional PM techniques. It is envisaged that testing and demonstration of RSB materials in the context of practical radiation shielding will be feasible in the near future. The main conclusions from this work are thus:

1. The Fe-rich interstitial phase was observed to consist of two Fe-based phases, one being a complex boron-rich Fe alloy of empirical composition $(Fe_{20}Cr_2)WB_4C_2$ alongside Cr,B,C-depleted Fe regions. No definitive evidence of iron borides was discovered in sintered RSBs, indicating that FeB_x is consumed by FeWB growth at liquid phase sintering. APT tomographs also show WC nuclei and Cr presence within the Fe-rich phase.
2. Carbon plays a critical role in determining the phase presence in sintered RSB materials and appears to play a role in limiting the consumption of WB/W_2B_5 and WC and preventing the runaway growth of $FeWB/FeW_2B_2$.
3. Cr mostly segregates into the $FeWB/FeW_2B_2$ or the Fe-rich interstitial phase modelled as $(Fe_{0.92}Cr_{0.08})_{22}B_4C_2W$ and behaves chemically similarly to Fe. There is a slight preference for Cr over Fe in W-rich environments. This has implications for altering the chemistry of RSBs when considering properties such as ferromagnetism in RSBs.
4. Combined boron and carbon content (B + C) at% determines whether an RSB composition forms a solid sintered body close to near net shape. Sintered RSBs did not form a coherent, dense body if (B + C) at% significantly less than 40%. Upper limit of (B + C) at% is assumed to be similar to that for cWC where the upper limit of C at% ≤ 48.5%. RSBs are predicted to form coherent sintered bodies if the condition 40% < (B + C) at% ≤ 50% is satisfied.
5. Delamination features on RSBs consistent with more gas evolution during sintering relative to cWCs. Increased gas evolution in RSBs relative to cWCs most probably results from increased oxygen content present in boron and boron-rich precursors.
6. Optimal RSB microstructures are anticipated to be composed of mixed, overlapping $FeWB/FeW_2B_2$ regions in a Fe-rich matrix forming a skeleton-like structure analogous to cWCs and would resemble a pore-free sample of composition B5T522W.

Acknowledgements,

J.M. Marshall would like to thank George Smith for help and advice on this work. Funding was provided by the EPSRC Early Career Fellowship EP/T033592/1 and the following people who contributed to this study:

References

[1] A. Sykes, A.E. Costley, C.G. Windsor, O. Asunta, G. Brittles, P. Buxton, V. Chuyanov, J.W. Connor, M.P. Gryaznevich, B. Huang, J. Hugill, A. Kukushkin, D. Kingham, A.V. Langtry, S. McNamara, J.G. Morgan, P. Noonan, J.S.H. Ross, V. Shevchenko, R. Slade, G. Smith, Compact fusion energy based on the spherical tokamak, Nucl. Fusion. 58 (2018) 016039. doi:10.1088/1741-4326/aa8c8d.

[2] P. Bruzzone, R. Wesche, D. Uglietti, N. Bykovsky, High temperature superconductors for fusion at the Swiss Plasma Center, Nucl. Fusion. 57 (2017). doi:10.1088/1741-4326/aa7bab.

[3] P. Bruzzone, W.H. Fietz, J. V. Minervini, M. Novikov, N. Yanagi, Y. Zhai, J. Zheng, High Temperature Superconductors (HTS) for Fusion Magnets, Nucl. Fusion. 58 (2018). doi:https://doi.org/10.1088/1741-4326/aad835.

[4] E. Surrey, Engineering challenges for accelerated fusion demonstrators, Philos. Trans. R. Soc. A Math. Phys. Eng. Sci. 377 (2019) 20170442. doi:10.1098/rsta.2017.0442.

[5] Y.K.M. Peng, D.J. Strickler, Features of spherical torus plasmas, Nucl. Fusion. 26 (1986) 769–777. doi:10.1088/0029-5515/26/6/005.

[6] A. Sykes, Progress on spherical tokamaks, Plasma Phys. Control. Fusion. 36 (1994). doi:10.1088/0741-3335/36/12B/007.

[7] A.E. Costley, J. Hugill, P.F. Buxton, On the power and size of tokamak fusion pilot plants and reactors, Nucl. Fusion. 55 (2015). doi:10.1088/0029-5515/55/3/033001.

[8] D.X. Fischer, R. Prokopec, J. Emhofer, M. Eisterer, The effect of fast neutron irradiation on the superconducting properties of REBCO coated conductors with and without arti fi cial pinning centers, Supercond. Sci. Technol. 31 (2018) 44006. doi:10.1088/1361-6668/aaadf2.

[9] S.A. Humphry-Baker, G.D.W. Smith, Shielding materials in the compact spherical tokamak, in: Philos. Trans. R. Soc. A Math. Phys. Eng. Sci., 2019: p. 20170443. doi:10.1098/rsta.2017.0443.

[10] H.L. Swami, C. Danani, A.K. Shaw, Activation characteristics of candidate structural materials for a near-term Indian fusion reactor and the impact of their impurities on design considerations, Plasma Sci. Technol. 20 (2018). doi:10.1088/2058-6272/aaabb4.

[11] C. Linsmeier, M. Rieth, J. Aktaa, T. Chikada, A. Hoffmann, J. Hoffmann, A. Houben, H. Kurishita, X. Jin, M. Li, A. Litnovsky, S. Matsuo, A. Von Müller, V. Nikolic, T. Palacios, R. Pippan, D. Qu, J. Reiser, J. Riesch, T. Shikama, R. Stieglitz, T. Weber, S. Wurster, J.H. You, Z. Zhou, Development of advanced high heat flux and plasma-facing materials, Nucl. Fusion. 57 (2017). doi:10.1088/1741-4326/aa6f71.

[12] C.G. Windsor, J.G. Morgan, P.F. Buxton, A.E. Costley, G.D.W. Smith, A. Sykes, Modelling the power deposition into a spherical tokamak fusion power plant, Nucl. Fusion. 57 (2017) 036001. doi:10.1088/1741-4326/57/3/036001.

[13] C.G. Windsor, J.M. Marshall, J.G. Morgan, J. Fair, G.D.W. Smith, A. Rajczyk-Wryk, J.M. Tarragó, Design of cemented tungsten carbide and boride-containing shields for a fusion power plant, Nucl. Fusion. 58 (2018). doi:10.1088/1741-4326/aabdb0.

[14] D. Hancock, D. Homfray, M. Porton, I. Todd, B. Wynne, Refractory metals as structural materials for fusion high heat flux components, J. Nucl. Mater. 512 (2018) 169–183. doi:10.1016/j.jnucmat.2018.09.052.

[15] X. Litaudon, JET Program for Closing Gaps to Fusion Energy, IEEE Trans. Plasma Sci. 44 (2016) 1481–1488. doi:10.1109/TPS.2016.2572158.

[16] A. Muller, B. Bosworth, V. Cerri, H. Gruener, R. Neu, Tungsten fibre-reinforced copper as an advanced heat sink material for highly heat loaded plasma-facing component, (2019). http://hdl.handle.net/21.11116/0000-0004-BCCF-0.

[17] G. Federici, W. Biel, M.R. Gilbert, R. Kemp, N. Taylor, R. Wenninger, European DEMO design strategy and consequences for materials, Nucl. Fusion. 57 (2017). doi:10.1088/1741-4326/57/9/092002.

[18] C.G. Windsor, J.G. Morgan, Neutron and gamma flux distributions and their implications for radiation damage in the shielded superconducting core of a fusion power plant, Nucl. Fusion. 57 (2017). doi:10.1088/1741-4326/aa7e3e.

[19] H. Wang, T. Webb, J.W. Bitler, Study of thermal expansion and thermal conductivity of cemented WC-Co composite, Int. J. Refract. Met. Hard Mater. 49 (2015) 170–177. doi:10.1016/j.ijrmhm.2014.06.009.

[20] P. Alexander, Atomic Radiation and Life, 2nd ed., Pelican, London, 1965.

[21] J.M. Marshall, EP3401413A1 “An iron tungsten borocarbide body for nuclear shielding applications,” (2018). doi:10.13140/RG.2.2.34460.13447.

[22] S.A. Humphry-Baker, J.M. Marshall, G.D.W. Smith, W.E. Lee, Thermophysical properties of Co-free WC-FeCr hardmetals, in: 19th Plansee Semin. 2017, 2017: pp. 1–13.

[23] J.M. Marshall, EP3401414A1. Cemented carbides comprizing a Fe-Cr binder metallic binder, (2019).

[24] J.M. Marshall, D. Walker, P.A. Thomas, HRXRD study of the Theoretical Densities of Novel Reactive Sintered Boride Candidate Neutron Shielding Materials, Nucl. Mater. Energy. (2020) 100732. doi:10.1016/j.nme.2020.100732.

[25] J.M. Marshall, M. Giraudel, The role of tungsten in the Co binder: Effects onWC grain size and hcp-fcc Co in the binder phase, Int. J. Refract. Met. Hard Mater. 49 (2015). doi:10.1016/j.ijrmhm.2014.09.028.

[26] J.M. Marshall, A. Kusoffsky, Binder phase structure in fine and coarse WC-Co hard metals with Cr and v carbide additions, Int. J. Refract. Met. Hard Mater. 40 (2013). doi:10.1016/j.ijrmhm.2013.04.001.

[27] G. Herranz, Control of carbon content in metal injection molding (MIM), Handb. Met. Inject. Molding. (2012) 265–304. doi:10.1533/9780857096234.2.265.

[28] B. Bakhit, D. Primetzhofer, E. Pitthan, M.A. Sortica, E. Ntemou, J. Rosen, L. Hultman, I. Petrov, G. Greczynski, Systematic compositional analysis of sputter-deposited boron-containing thin films, J. Vac. Sci. Technol. A. 39 (2021) 063408. doi:10.1116/6.0001234.

[29] R.A. Young, The Rietveld Method, 1995th ed., Oxford University Press, Oxford, 1993.

[30] S.S. Setayandeh, E.G. Obbard, J.H. Stansby, D. Frost, O. Jack, C.L. Wilson, P.A. Burr, A DFT study to determine the structure and composition of ε -W 2 B 5-x, J. Alloys Compd. 911 (2022) 164962.

[31] M.A. Yousfi, S. Norgren, H.O. Andrén, L.K.L. Falk, Chromium segregation at phase boundaries in Cr-doped WC-Co cemented carbides, Mater. Charact. 144 (2018) 48–56. doi:10.1016/j.matchar.2018.06.034.

[32] J. García, S. Englund, F. Haglöf, Controlling cobalt capping in sintering process of cermets, Int. J. Refract. Met. Hard Mater. 62 (2017) 126–133. doi:10.1016/j.ijrmhm.2016.06.008.

[33] R. Frykholm, M. Ekroth, B. Jansson, H.O. Andrén, J. Ågren, Effect of cubic phase composition on gradient zone formation in cemented carbides, Int. J. Refract. Met. Hard Mater. 19 (2001) 527–538. doi:10.1016/S0263-4368(01)00043-9.

[34] E.A. Álvarez, C.J.R.G. Oliver, J.L. García, Densification and Phase Formation Kinetics in Composite Materials of WC Embedded in an Fe-Matrix, Procedia Mater. Sci. 9 (2015) 13–20. doi:10.1016/j.mspro.2015.04.003.

[35] J. Li, J. Li, C. Li, Y. Liu, Reactive synthesis of FeWB powders and preparation of bulk materials, Int. J. Refract. Met. Hard Mater. 46 (2014) 80–83. doi:10.1016/j.ijrmhm.2014.05.011.

[36] L.G. Yu, X.J. Chen, K.A. Khor, G. Sundararajan, FeB/Fe2B phase transformation during SPS pack-boriding: Boride layer growth kinetics, Acta Mater. 53 (2005) 2361–2368. doi:10.1016/j.actamat.2005.01.043.

[37] O. Delai, C. Xia, L. Shiqiang, Growth kinetics of the FeB/Fe2B boride layer on the surface of 4Cr5MoSiV1 steel: Experiments and modelling, J. Mater. Res. Technol. 11 (2021) 1272–1280. doi:10.1016/j.jmrt.2021.01.109.

[38] H. Mohebbi, D.A. Jesson, M.J. Mulheron, P.A. Smith, The fracture and fatigue properties of cast irons used for trunk mains in the water industry, Mater. Sci. Eng. A. 527 (2010) 5915–5923. doi:10.1016/j.msea.2010.05.071.

[39] B. Roebuck, Terminology, testing, properties, imaging and models for fine grained hardmetals, Int. J. Refract. Met. Hard Mater. 13 (1995) 265–279. doi:10.1016/0263-4368(95)92673-8.

[40] E. Zhao, J. Meng, Y. Ma, Z. Wu, Phase stability and mechanical properties of tungsten borides from first principles calculations, Phys. Chem. Chem. Phys. 12 (2010) 13158–13165. doi:10.1039/c004122j.

[41] M. Athanasakis, E. Ivanov, E. del Rio, S.A. Humphry-Baker, A high temperature W$_2$B cermet for compact neutron shielding, J. Nucl. Mater. 532 (2020) 1–10. http://arxiv.org/abs/1912.04671.

[42] R.Karre, Y. Hu , S. Song, X. Wang, J. Joardar,K. M. Reddy, Observations of multi-component boride precipitates in ultrahard boron carbide Mat. Character. 176 (2021) 111106

[43] H. Itoh, T. Matsudaira, S. Naka, H. Hamamoto, M. Obayashi, Formation process of tungsten borides by solid state reaction between tungsten and amorphous boron, J. Mater. Sci. 22 (1987) 2811–2815. doi:10.1007/BF01086475.

Fig. 1. SEM-EDX maps from RSB sample B5T522W. **a** SE image with combined X-ray maps, **b** B Kα1-2, **c** C Kα1-2, **d** Cr Kα, **e** W Lα1 and **f** Fe Kα1. Preliminary phase fields identified are (1) Tungsten Boride WB/W_2B_5; (2) FeWB, FeW_2B_2; (3) Iron boride and (4) C-rich simple borides and carbides around pores. Another Fe-dominant **(f)** region is defined by Cr and B depletion relative to other Fe-rich regions (**d** and **f)**.

Fig. 2. SEM-EDX maps from RSB composition B7TE23W. **a** SE image with combined X-ray maps for B7TE23W, **b** B Kα1-2, **c** C Kα1-2, **d** Cr Kα, **e** W Lα1 and **f** Fe Kα1. Only 2 main phases are present (2) FeWB and (3) Fe-rich/Fe.

Fig. 3. a SE image with combined X-ray maps for B9TE25W, **b** C Kα1-2, **c** Fe Kα1, **d** Cr **e** W Lα1 and **f** Fe Kα1. The same phases are present as seen in **Fig. 1.** with the possible addition of mixed metal carbides $Fe_3C/M_{12}C$ (1) Tungsten Boride WB/W_2B_5; (2) FeWB; (3) Iron boride and (4) C-rich simple borides and carbides around pores.

Fig. 4. a BF-STEM image, **b** ADF-STEM image and **(c-h)** TEM-EDX elemental maps from RSB composition B5T522W. EDX maps extracted from **c** B-Kα, **d** C-Kα, **e** Cr-Kα, **f** W-Lα, **g** Fe-Kα and **h** DF image overlayed with region key: (1)WC, (2)W_2B_5/WB, (3)WB, (4)FeWB/FeW_2B_2, (5)Pure Fe (Cr-depleted)(6) $Fe(B,C)_x$, (T) Thicker region. Ringed area in **a** shows the $Fe(B,C)_x$/Fe interface. Images **i** and **j** show evidence of mixed WC/W_2B_5 epitaxy **i** from the textured appearance in region (1/2) and a small C-rich crystal (7) present in **b**.

Fig. 5. APT tip location on RSB sample **a** prior to FIB/Pt deposition and **b** Pt-coated cantilever prior to sectioning and shaping.

Fig. 6. Atom probe data from Tip 4. **a** SEM image of FIB-milled tip **b** APT reconstruction and **c** mass-to-charge-state ratio spectrum.

Fig. 7. Atom probe data from Tip 1. **a** SEM image of FIB-milled tip **b** APT reconstruction and **c** mass-to-charge-state ratio spectrum.

Fig. 8. TOPAS model of complex as $(Fe_{0.92}Cr_{0.08})_{22}B_4C_2W$. Fe(Cr)1 has occupancy of $Fe_{0.9}Cr_{0.06}$ and Fe(Cr)2 has occupancy of $Fe_{0.9}Cr_{0.1}$ respectively. Silver sites are the shared $W_{0.43}Cr_{0.57}$ site with B and C sharing the original B site.

Fig.9. X-ray model fits of RSB surface spectra from **a** composition B5T522W, **b** B7TE23W and **c** B9TE25W. Fits show (i) models using iron borides and (ii) models using the bcc (Fe, Cr)(B, C) ($(Fe_{20}Cr_2W)B_4C_2$) Fe-rich alloy discovered from APT analysis. For clarity, only peaks in the solid spectra differing from the powder data are labeled.

Declaration of interests

☐ The authors declare that they have no known competing financial interests or personal relationships that could have appeared to influence the work reported in this paper.

☒ The authors declare the following financial interests/personal relationships which may be considered as potential competing interests:

Jessica Marshall has patent # WO2018206174A1. "Cemented carbides comprizing a Fe-Cr binder metallic binder" issued to Sandvik Hyperion AB (Hyperion MT as of 2018). Jessica Marshall has patent #WO2018206173A1 "An iron tungsten boride body for nuclear shielding applications " issued to Sandvik Hyperion AB (Hyperion MT as of 2018).

Credit statement for ”Multi-Scale Microscopy of Reactive Sintered Boride (RSB) Neutron Shielding Materials”

J. M. Marshall	Conceptualization, Funding acquisition Methodology, Validation and Original draft writing.
P. A. J. Bagot	Investigation, data curation, Formal analysis, Methodology, proofreading
M. P. Moody	Investigation, data curation, Formal analysis, Methodology, proofreading
Yisong Han	Investigation, Methodology, proofreading
Fengzai Tang	Investigation, Methodology.

Acknowledgements:

G.D.W. Smith for commentary and editorial support for this manuscript.

Funding source: EPRSC ECR Fellowship [EP/T033592/1]

- Porosity in RSB materials result of more outgassing during sintering than for cWCs.
- Iron tungsten borides can form a cohesive network of bodies 10 - 100 μm diameter.
- Cr behaves chemically as Fe with Cr segregating to any Fe and W-containing phase.
- Cohesive, tractable RSB materials do not form when (B + C) at% < 40% .
- Two distinct Fe-rich phases: A (Fe,Cr)(B,C) alloy and a Cr-depleted Fe phase.